Nanoscale

Accepted Manuscript

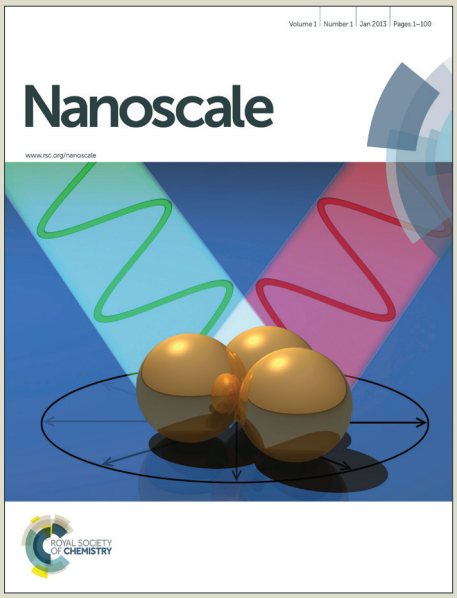

Cite this: DOI: 10.1039/c0xx00000x

www.rsc.org/xxxxxx

Communication

Monodisperse Sr-La_2O_3 hybrid nanofibers for oxidative coupling of methane to synthesize C_2 hydrocarbons

Jianjun Song,[a,b] Yongnan Sun,[a,c] Rongbin Ba,[a,b] Shangshang Huang,[a,b] Yonghui Zhao,[a] Jun Zhang,[a] Yuhan Sun[a,*] and Yan Zhu[a,*]

Received (in XXX, XXX) Xth XXXXXXXXX 20XX, Accepted Xth XXXXXXXXX 20XX
DOI: 10.1039/b000000x

The synergistic effects from combinations of each component's functionality in hybrid Sr-La_2O_3 nanofibers brought about an improved catalytic behaviour for oxidative coupling of methane carried out under high temperature, which cannot be achieved over the conventional Sr doped La_2O_3 spherical catalyst.

Hybrid nanocatalysts with different component arranged in a controlled structure are widely used in industry since they can provide entirely novel activity and selectivity for many important chemical reactions via the coupling between components within the hybrids.[1-3] This class of hybrid nanomaterials combines dissimilar materials into a single multifunctional fashion, and facilitates the electron or charge and energy flow between constituent hybrids.[4-6] Different functionalities from each component of hybrids can be integrated to bring about a synergistic effect and new functionality, so the hybrid nanocatalysts are desirable for catalytic reaction.[7,8] Progress in nanomaterial synthesis has made it possible for synthetic strategies of hybrid nanomaterials, such as metal oxide-metallic,[6,9] semiconductor-metallic[10] and semiconductor-magnetic hybrid nanomaterials.[11] However, most of these hybrid nanomaterials are used under mild reaction conditions and it remains unclear whether hybrid nanomaterials are stable when they are used as catalysts for the high temperature reactions since one component as a dopant is very mobile and easy to remove from the hybrids under high temperature conditions.[12] Especially, direct conversion of CH_4 to form chemicals such oxidative coupling of methane (OCM) is difficult succeeded at mild conditions, and the activation of CH_4 to methyl radical by the abstraction of H-atom at the aid of O_2 and the coupling of methyl radicals to form C_2 hydrocarbons (ethane/ethene) is carried out under high temperature (~ 800 ^oC).[12-15] The severe high temperature condition could lead to the complete oxidization of methane to produce CO and CO_2, and moreover suppress the selectivity of C_2 hydrocarbons.[16,17] Thanks to the discovery in previous investigation that La_2O_3 nanorods exhibited low ignition temperature (450 ^oC) of CH_4 compared with corresponding nanoparticles,[18] it is now possible for precise synthesis of metal-inserted La_2O_3 hybrid nanofibers by a facile route for OCM reaction.

In the present work, we report, for the first time, the target-specific synthesis of monodisperse hybrid Sr-La_2O_3 nanofibers through an incipient wetness impregnation route. Sr-La_2O_3 nanofibers acted as a catalyst for oxidative coupling of methane, unprecedented in the literatures, the initial ignition temperature of methane is about 500 ^oC, and the conversion of methane and the selectivity of C_2 hydrocarbons could be up to ~35% and 47% at 500 ^oC (Figure 1), respectively. Within these hybrid Sr-La_2O_3 nanofibers, 8.6 wt% Sr-La_2O_3 nanofibers (the content of Sr is 8.6 wt%) exhibited the highest methane conversion and C_2 selectivity, in particular, 20% yield towards C_2 hydrocarbons was obtained at 650 ^oC (Figure 1b), which cannot be achieved over conventional Sr doped La_2O_3 spherical catalysts (Figure S1). More ethene and ethane can be produced on the Sr-La_2O_3 nanofiber than pure La_2O_3 (Figure 1c). The complete oxdiation products like CO and CO_2 can be suppressed on Sr-La_2O_3 nanofibers (Figure 1d). Other metals such as Ba, Ca and K modified La_2O_3 nanofibers can not exhibit superior catalysis to Sr-La_2O_3 nanofibers for OCM reactions (Figure S2). Additionally, the hybrid Sr-La_2O_3 nanofibers showed a good stability during the oxidative coupling of methane at temperatures tested, which can be inferred from the stability test under different reaction conditions. From Figure S3, it was found that the conversion of CH_4 and yield of C_2 decreased slightly during the 100 hours test. The improved activity and selectivity over Sr-La_2O_3 nanofibers are attributed to the synergistic effect of material properties of individual Sr and La_2O_3 optimized independently, such Sr might tailor the lattice structure and electronic structure of La_2O_3, change the oxygen species and basic sites on the surface of La_2O_3, and lower the reaction energy of CH_4 on the surface of hybrid catalysts, which have been revealed by our studies.

[a] *CAS Key Laboratory of Low-Carbon Conversion Science and Engineering, Shanghai Advanced Research Institute, Chinese Academy of Sciences, Shanghai 201210, China. E-mail: zhuy@sari.ac.cn; sunyh@sari.ac.cn*
[b] *University of Chinese Academy of Sciences, Beijing 100049, China.*
[C] *Department of Materials and Science and Engineering, Shanghai University, shanghai, 200444, china.*
† Electronic Supplementary Information (ESI) available: [details of any supplementary information available should be included here]. See DOI: 10.1039/b000000x/

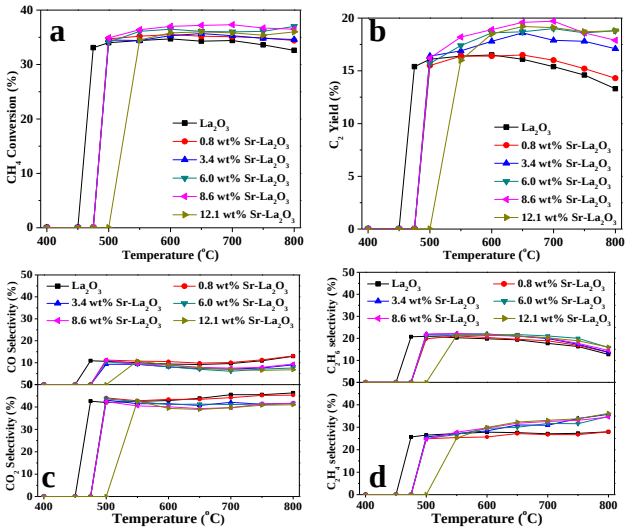

Figure 1. Catalytic performances of pure La_2O_3 and hybrid Sr-La_2O_3 nanofibers for OCM reaction. Upper panel and lower panel of c are C_2H_6 selectivity and C_2H_4 selectivity. Upper panel and lower panel of d are CO selectivity and CO_2 selectivity.

We now turn to the studies to find the reasons why the hybrid Sr-La_2O_3 nanofibers have an improved catalytic performance and good stability, compared to pure La_2O_3 nanofibers. Firstly, TEM, XRD and theoretic studies confirmed that the lattice structure of La_2O_3 can be indeed tailored by the Sr insert. Pure La_2O_3 nanofibers were 20-30 nm in diameter and several micrometers in length with smooth surfaces (Figure 2a). Herein, 8.6 wt% Sr-La_2O_3 nanofibers as an example, hybrid Sr-La_2O_3 nanofibers with rough surface were in a diameter of 40-50 nm with hundreds nanometers in length (Figure 2b and 3a). The corresponding EDS analysis shown in the inset of Figure 2b, was a direct evidence to let us believe the existence of Sr in hybrid nanofibers. The homogeneous distribution of Sr in hybrid nanofibers was presented in the element mapping (Figure 3d), which clearly revealed the existence and distribution of Sr, La and O elements in hybrid nanofibers, wherein different colors represented different elements (Figure 3b-d). Unlike conventional Sr doped La_2O_3 spherical catalyst, Sr easily leaking from the doped catalyst under high temperature conditions, hybrid Sr-La_2O_3 catalysts are much stable during the OCM reaction and Sr element was still homogeneous distributed in hybrid nanofibers after reaction, as shown in Figure 3e-h. Especially, TG-MS data of spent Sr-La_2O_3 catalyst indicated that no coke was formed on hybrid Sr-La_2O_3 nanofibers, verified by no weight loss measured from spent catalyst (Figure S4). It is of paramount importance to attain the catalytic materials which can resist sintering and coking at high temperature.

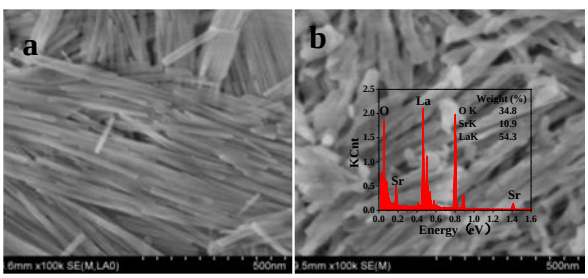

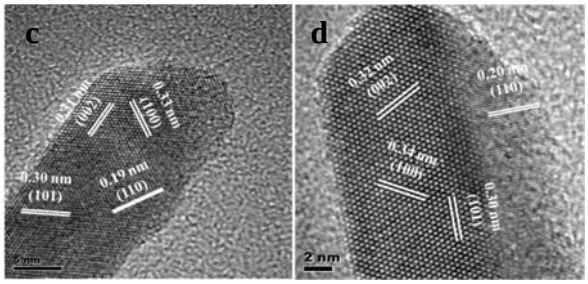

Figure 2. SEM images of (a) pure La_2O_3 and (b) Sr-La_2O_3 nanofibers, and the inset is corresponding EDS data. HRTEM images of (c) pure La_2O_3 nanofibers and (d) Sr-La_2O_3 nanofibers.

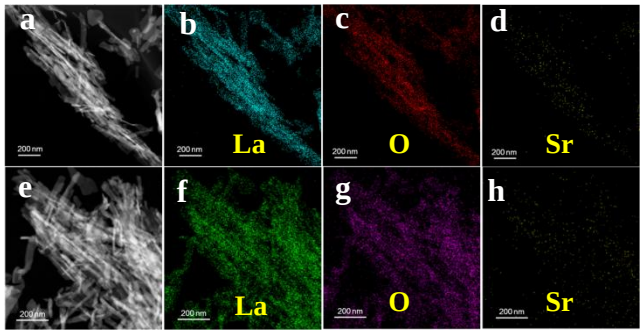

Figure 3. (a) TEM image of fresh Sr-La_2O_3 nanofibers and (b, c, d) the corresponding element maps for La, O and Sr. (e) TEM image of spent Sr-La_2O_3 nanofibers and (f, g, h) the corresponding element maps for La, O and and Sr.

Moreover, the introduction of Sr widened the lattice fringes of La_2O_3 nanofibers. In Figure 2c, the crystal lattice fringes of La_2O_3 are 0.19, 0.30, 0.31 and 0.33 nm apart, which agree with the *d* value of (110), (101), (002) and (100) lattice planes of hexagonal La_2O_3 with growth along the (101) direction. For Sr-La_2O_3 nanofibers, the crystal lattice fringes of La_2O_3 are 0.20, 0.30, 0.32 and 0.34 nm apart, which are corresponding to the *d* value of (110), (101), (002) and (100) lattice planes of hexagonal La_2O_3. The lattice fringes of (110), (101) and (002) lattice planes broaden after introducing Sr, which is due to the ionic larger radii of Sr (0.118Å) than La ions (0.1032Å).

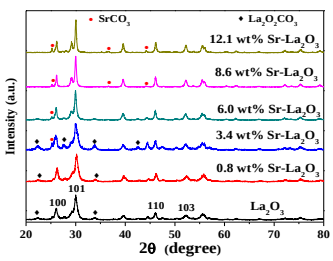

catalyst	*a* (Å)	*b* (Å)	*c* (Å)
La_2O_3	0.3930	0.3930	0.6109
0.8 wt % Sr/ La_2O_3	0.3930	0.3930	0.6109
3.4 wt % Sr/ La_2O_3	0.3934	0.3934	0.6117
6.0 wt % Sr/ La_2O_3	0.3934	0.3934	0.6117
8.6 wt % Sr/ La_2O_3	0.3934	0.3934	0.6117
12.1 wt % Sr/ La_2O_3	0.3934	0.3934	0.6117

Figure 4. XRD patterns of La_2O_3 and Sr-La_2O_3 nanofibers (left panel) and lattice parameters (*a*, *b* and *c*) of La_2O_3 and Sr-La_2O_3 nanofibers (right panel).

XRD studies further corroborated the change of space lattice of La_2O_3 nanofibers via the insert of Sr ions into the crystal lattice of La_2O_3 (right panel of Figure 4). Without Sr inserted, the lattice parameters of hexagonal La_2O_3 is 0.3930 Å (*a*), 0.3930 Å (*b*) and 0.6109 Å (*c*), while hybrid Sr-La_2O_3, in particular the Sr content is equal to or more than 3.4 wt%, the lattice parameters of La_2O_3 are broadened such 0.3934 Å (*a*), 0.3934 Å (*b*) and 0.6117 Å (*c*),

respectively. Interestingly, XRD patterns of pure La_2O_3 and hybrid Sr-La_2O_3 nanofibers showed the similar diffraction peaks at 2θ = 26.11°, 29.96°, 46.08°, and 52.13°, corresponding to the characteristic diffractions of the (100), (101), (110), and (103) planes of La_2O_3 (JCPDS 05-0602). It is noted that black rhombs in the XRD of Figure 4 referred to the $La_2O_2CO_3$ phases, which cannot be avoided for La_2O_3 to transform into $La_2O_2CO_3$ in moist air. Red dots in the left panel of Figure 4 stood for the $SrCO_3$ phases, which might be generated during the calcination of $Sr(NO_3)_2$-$La(OH)_3$ in the air (experimentals in Supporting Information). Thus these catalysts must be pretreated at 800°C under N_2 for 2 h before OCM test to remove these impurities. There is no indication of Sr or related oxide phases, suggesting the single component of Sr-La_2O_3 themselves rather than the mix of Sr and La_2O_3, except for small amount of $SrCO_3$ and $La_2O_2CO_3$. After reaction, the spent Sr-La_2O_3 showed similar XRD diffractions of fresh catalysts (Figure S5).

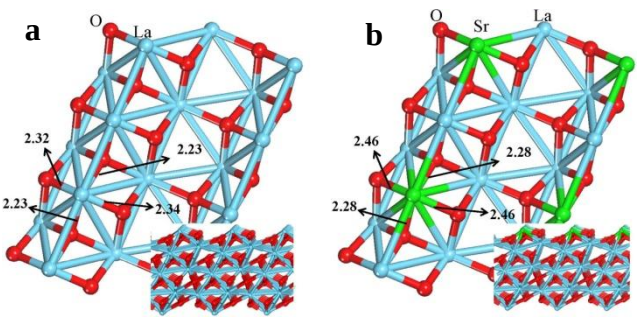

Figure 5. The side and top views of (a) pure La_2O_3(101) surfaces and (b) hybrid Sr-La_2O_3(101) surfaces.

The change of La_2O_3 structure caused via inserting Sr was also confirmed by DFT + U method (the periodic plane wave DFT implementation in the Vienna ab initio simulation program (VASP) code [19,20]). For the La f orbitals, a value of 7.5 eV for the U parameter for all calculations was presented herein as suggested in the literature.[21] The side and the top views of the pure and hybrid Sr-La_2O_3 (101) surfaces, and the optimized bond length for the top layer atoms (eg. La-O and O-Sr) are shown in Figure 5. The optimized La atom in the surface layer of the La_2O_3 (101) face is coordinated with four O atoms, with La-O distances of 2.23, 2.23, 2.34 and 2.32 Å (Figure 5a). With Sr introduction, there are corresponding four Sr-O, with Sr-O distances of 2.28, 2.28, 2.46 and 2.46 Å (Figure 5b). From the values, the expanding in the structure caused by Sr is obvious and such change in the structure should result in a difference in the activity of hybrid Sr-La_2O_3 and pure La_2O_3.

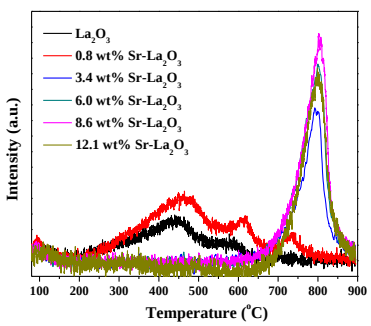

Figure 6. CO_2-TPD profiles of pure La_2O_3 and hybrid Sr-La_2O_3 nanofibers.

Besides the surface structure of La_2O_3 tailored by Sr, the surface species and surface basic sites on the Sr-La_2O_3 face made such a difference to that of pure La_2O_3. The characterization from CO_2-TPD allowed us to demonstrate the nature of surface strong basic site on Sr-La_2O_3 nanofibers (Figure 6). There are three types of basic sites: the weak, medium and strong basic site, which are associated with desorption of CO_2 at the temperatures 100 °C, 300-600 °C and >600 °C, respectively. Among the three distinct basic sites, the strong basic sites are crucial for the OCM process carried out above 600 °C. The addition of Sr, influencing sharply the strength and quantity of base of La_2O_3, resulted in the creation of more strong basic sites compared with intermediate basic sites. For pure La_2O_3, most of CO_2 was desorbed at 300-600 °C. For 0.8 wt% Sr-La_2O_3, partial of CO_2 was desorbed at >600 °C, and most CO_2 was desorbed at 300-600 °C. When the Sr content exceeded 3.4 wt% within hybrids, almost all of CO_2 was desorbed at 700-800 °C. It suggests that the surfaces of La_2O_3 and 0.8 wt% Sr-La_2O_3 are dominated by medium basic site, whereas the surface of Sr-La_2O_3 with Sr content above 3.4 wt% are dominated by strong basic site. The distinct difference of basic sites on the surfaces is one of reasons for improved catalysis of hybrid Sr-La_2O_3 on OCM reaction.

Table 1. Curve-Fitting results from XPS Data

Catalysts	O 1s binding energies (eV)				$(O^-+O_2^-)/O^{2-}$
	O^{2-}	O^-	CO_3^{2-}	O_2^-	
La_2O_3	529.1	531.5	532.7	534.6	5.1
0.8 wt% Sr-La_2O_3	529.1	531.0	532.1	533.6	3.4
3.4 wt% Sr-La_2O_3	528.7	531.1	531.9	534.0	4.3
6.0 wt% Sr-La_2O_3	528.7	531.1	532.0	533.9	4.6
8.6 wt% Sr-La_2O_3	529.1	531.6	533.0	534.6	7.5
12.1 wt% Sr-La_2O_3	528.9	531.1	532.1	533.4	5.1

The roles played by surface oxygen species are, in addition to surface basic sites, investigated by XPS analyses. The O1s spectra of samples can be deconvoluted into four peaks corresponding to four different oxygen species: superoxide O_2^-; carbonate CO_3^{2-}; peroxide ions O^-; and lattice oxygen O^{2-}, seen in Table 1. The electron deficient species such O_2^- and O^- on the surface of catalysts, as is well-known, are effective for the C_2 selectivity, while the lattice oxygen O^{2-} is responsible for complete oxidation to form CO and CO_2.[18,22] The ratio of the peak intensities of the electron deficient species to lattice oxygen, $(O_2^-+O^-)/O^{2-}$, can be calculated using the 80% Gaussian-20% Lorentzian peak shape (Figure S6). From the ratio values of $(O^-+O_2^-)$ to O^{2-} shown in Table 2, 8.6 wt % Sr-La_2O_3 nanofibers have the highest ratio value (7.5) and achieved the highest C_2 selectivity among the hybrid catalysts, which is in accordance with literatures.[18,22]

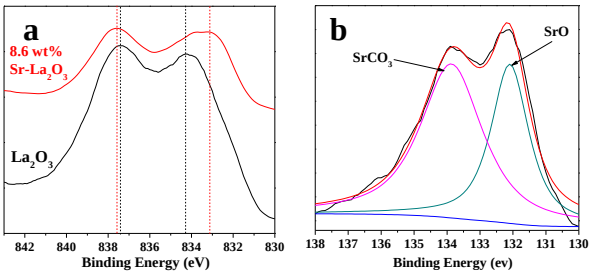

Figure 7. (a) XPS La $3d_{5/2}$ spectra of La_2O_3 and 8.6 wt% Sr-La_2O_3 nanofibers and (b) Sr 3d XPS spectra of 8.6 wt% Sr-La_2O_3.

Figure 7 (curve a) showed the typical La $3d_{5/2}$ of pure La_2O_3 and 8.6 wt% Sr-La_2O_3 nanofibers. After the introduction of Sr, the binding energy peak located at 834.3 eV moved to a lower binding energy (833.1 eV), and the energy peak at 837.4 eV shifted to a higher binding energy (837.5 eV), revealing that the electronic properties of La was changed by Sr insert. Figure 7b showed that the Sr 3d spectra could be divided into two peaks at the binding energy of 132.1 eV and 133.9 eV, which are corresponding to SrO and $SrCO_3$,[23] suggesting that Sr occurred on the surface of Sr-La_2O_3 in the form of SrO and $SrCO_3$.

The comparison of the structure and energetics of the associative and dissociative adsorption of CH_4 on pure and hybrid Sr-La_2O_3 could be made through DFT study, since the reaction pathway of CH_4 on the two catalysts is difficultly traced. The optimized structures for the CH_4, CH_3, H and co-adsorbed CH_3+H on Sr-La_2O_3(101) surfaces were shown in Figure 8, and distances for H-O and C-O were listed in Table 3. In Figure 8, CH_3, H are preferable to be adsorbed at the three bonded oxygen near Sr atom. Corresponding optimized structures for the CH_4, CH_3, H and co-adsorbed CH_3+H on pure La_2O_3(101) surfaces can get from our former work.[18] The adsorption energies for all the species on the pure La_2O_3 surface are all weaker than those of Sr-La_2O_3 surface (-0.11 vs. -0.12 eV for CH_4, -2.34 vs. -3.54 eV for CH_3, and -3.40 vs. -4.67 eV for H). The interatomic distances between O and H, O and C on the Sr-La_2O_3(101) surfaces are all shorter than the pure La_2O_3 surface (2.23 vs. 2.33 Å for CH_4, 0.96 vs. 0.97 Å for H, and 1.39 vs. 1.40 Å for CH_3). The same trends are observed in the CH_3 + H co-adsorption, with adsorption energies of -4.54 eV and -6.97 eV, respectively. Thus, the corresponding reaction energies of CH_4 activation on (101) of La_2O_3 and Sr-La_2O_3 are 0.30 and -2.13 eV, respectively. According to the Brønsted–Evans–Polanyi relationship, such significant difference (2.43 eV) in reaction energy suggests that methane activation is preferred over the (101) surface of Sr-La_2O_3, even when taking the actual reaction conditions into account.

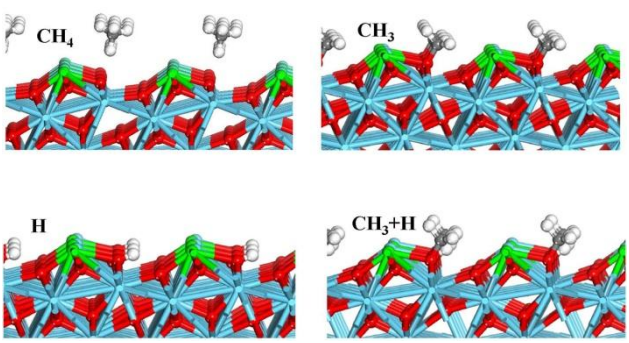

Figure 8. The optimized structures for the CH_4, CH_3, H and co-adsorbed CH_3+H on Sr-La_2O_3(101) surfaces.

Table 2. Adsorption energies, structure parameters of CH_4, CH_3, H and co-adsorbed CH_3+H on pure La_2O_3 (101) surfaces and Sr-La_2O_3 (101) surfaces.

Adsorbates	Surface	Eads/eV	d_{O-H}(Å)	d_{C-H}(Å)
CH_4	La_2O_3(101)	-0.11		2.33
	Sr-La_2O_3(101)	-0.12		2.23
CH_3	La_2O_3(101)	-2.34		1.40
	Sr-La_2O_3(101)	-3.54		1.39
H	La_2O_3(101)	-3.47	0.97	
	Sr-La_2O_3(101)	-4.67	0.96	
CH_3+H	La_2O_3(101)	-4.54	0.98	1.41
	Sr-La_2O_3(101)	-6.97	0.97	1.39

Conclusions

In summary, hybrid Sr-La_2O_3 nanofibers enhanced significantly conversion of CH_4 and the selectivity of C_2 hydrocarbons. Especially, for 8.6 wt% Sr-La_2O_3 hybrid catalyst, the initial ignition temperature of methane was about 500°C, and methane conversion and C_2 selectivity were up to ~35% and 47% at 500°C. The synergistic effects of material properties of individual Sr and La_2O_3 optimized independently, *i.e.* lattice structure and electronic properties of La_2O_3 are tailored by Sr, surface basic sites of La_2O_3 are strengthened by Sr, oxygen species on the surface of La_2O_3 are modified by Sr, and methane activation is preferred over Sr-La_2O_3 surface, are believed to be primarily responsible for the improved activity and selectivity over Sr-La_2O_3 nanofibers. Especially, Sr-La_2O_3 nanofibers have the ability to resist sintering and further avoid the loss of Sr, as well as no coke is formed on the surface of Sr-La_2O_3 catalysts during the high temperature reaction. As we have seen, the Sr-La_2O_3 nanocatalysts may open an avenue for a new type hybrid catalyst with high activity and selectivity for oxidative coupling of methane carried out at high temperature, and are promising in that they will provide new opportunities for studying the nature of hybrid catalysts for high temperature reaction.

Acknowledgments

The work was supported by National Natural Science Foundation (21273151, 21403277), Shanghai Pujiang Program (13PJ1407700), Shell Global Solutions International B. V. and Hundred Talent Program of CAS. We thank Dr. Carl Mesters and Dr. Alexander van der Made from Shell for helpful discussions.

Notes and references

1. A. Azetsu, H. Koga, A. Isogai and T. Kitaoka, *Catalysts*, 2011, **1**, 83-96.
2. F. Alosfur, M. H. H. Jumali, S. Radiman, N. J. Ridha, M. A. Yarmo and A. A. Umar, *Int. J. Electro. Sci.*, 2013, **8**, 2977-2982.
3. Y. Lu, Y. Jiang, X. Gao, X. Wang and W. Chen, *J. Am. Chem. Soc.*, 2014, **136**, 11687-11697.
4. L. L. Chng, N. Erathodiyil and J. Y. Ying, *Acc. Chem. Res.*, 2013, **46**, 1825-1837.
5. M. N. Luwang, S. Chandra, D. Bahadur and K. Srivastava, *J. Mater. Chem.*, 2012, **22**, 3395-3403.
6. R. Ferrando, G. Rossi, F. Nita, G. Barcaro and A. Fortunelli, *ACS Nano*, 2008, **2**, 1849-1856.

7. J. Guo, H. Li, H. He, D. Chu and R. Chen, *J. Phys. Chem. C*, 2011, **115**, 8494-8502.
8. S. Chen, R. Si, E. Taylor, J. Janzen and J. Chen, *J. Phys. Chem. C*, 2012, **116**, 12969-12976.
9. S. Liu, S.-Q. Bai, Y. Zheng, K. W. Shah and M.-Y. Han, *ChemCatChem*, 2012, **4**, 1462-1484.
10. K. Maeda, K. Sekizawa and O. Ishitani, *Chem. Commun.*, 2013, **49**, 10127-10129.
11. M. Casavola, V. Grillo, E. Carlino, C. Giannini, F. Gozzo, E. Fernandez Pinel, M. Angel Garcia, L. Manna, R. Cingolani and P. Davide Cozzoli, *Nano Lett.*, 2007, **7**, 1386-1395.
12. S. Arndt, G. Laugel, S. Levchenko, R. Horn, M. Baerns, M. Scheffler, R. Schloegl and R. Schomaecker, *Catal. Rev.*, 2011, **53**, 424-514.
13. T. Ito, J. X. Wang, C. H. Lin and J. H. Lunsford, *J. Am. Chem. Soc.*, 1985, **107**, 5062-5068.
14. J. E. France, A. Shamsi and M. Q. Ahsan, *Energy & Fuels*, 1988, **2**, 235-236.
15. M. T. Xu and J. H. Lunsford, *Catal. Lett.*, 1991, **11**, 295-300.
16. J. H. Lunsford, *Angew. Chem. Int. Ed.*, 1995, **34**, 970-980.
17. J. L. Dubois and C. J. Cameron, *Appl. Catal.*, 1990, **67**, 49-71.
18. P. Huang, Y. Zhao, J. Zhang, Y. Zhu and Y. Sun, *Nanoscale*, 2013, **5**, 10844-10848.
19. G. Kresse and J. Furthmuller, *Phys. Rev. B*, 1996, **54**, 11169-11186.
20. G. Kresse and J. Hafner, *Phys. Rev. B*, 1994, **49**, 14251-14269.
21. B. Li and H. Metiu, *J. Phys. Chem. C*, 2010, **114**, 12234-12244.
22. W. P. Ding, W. P. Ding, Y. Chen and X. C. Fu, *Catal. Lett.*, 1994, **23**, 69-78.
23. M. V. Bukhtiyarova, A. S. Ivanova, L. M. Plyasova, G. S. Litvak, V. A. Rogov, V. V. Kaichev, E. M. Slavinskaya, P. A. Kuznetsov and I. A. Polukhina, *Appl. Catal. A*, 2009, **357**, 193-205.